

Comparison of Sulfur Incorporation into CuInSe_2 and CuGaSe_2 Thin-Film Solar Absorbers

Faraz Khavari,* Jan Keller, Jes K. Larsen, Kostiantyn V. Sopiha, Tobias Törndahl, and Marika Edoff

Herein, sulfurization of CuInSe_2 and CuGaSe_2 (CGSe) absorber layers is compared to improve the understanding of sulfur incorporation into Cu(In,Ga)Se_2 films by annealing in a sulfur atmosphere. It is found for Cu-poor CuInSe_2 that for an annealing temperature of 430 °C, sulfur is incorporated into the surface of the absorber and forms an inhomogeneous CuIn(S,Se)_2 layer. In addition, at 530 °C, a surface layer of CuInS_2 is formed. In contrast, for Cu-poor CuGaSe_2 samples, S can only be introduced at 530 °C, mainly forming an alloy of CuGa(S,Se)_2 , where no closed CuGaS_2 layer is found. In Cu-rich CuGaSe_2 samples, however, selenium is substituted by S already at 330 °C, which can be explained by a rapid phase transformation of Cu_{2-x}Se into $\text{Cu}_{2-x}(\text{S,Se})$. This transformation facilitates S in-diffusion and catalyzes CuGa(S,Se)_2 formation, likewise that previously reported to occur in CuInSe_2 . Finally, the Cu-poor CuInSe_2 solar cell performance is improved by the sulfurization step at 430 °C, whereas for the 530 °C sample, a decreasing fill factor and short-circuit current density are observed, indicating lower diffusion length accompanied by possible formation of an electron transport barrier. In contrast, the electrical characteristics deteriorate for all sulfurized Cu-poor CuGaSe_2 cells.

recombination in these defect-rich areas. A GGI grading can be implemented during co-evaporation of the CIGSe absorber, which widens the bandgap toward the molybdenum back contact by shifting the conduction band upward.^[4] An SSSe grading is usually obtained by adding S in a sequential absorber deposition process such as sulfurization-after-selenization^[3] or annealing of stacked-elemental layers in S-containing atmosphere.^[5] In both methods, sulfur is added during the baseline processing, which is claimed to enable the formation of a CIGSSe alloy at the absorber surface. The main aim of a surface SSSe grading is to increase the bandgap energy near the absorber/buffer interface via shifting the conduction band minimum upward and lowering of the valence band maximum,^[6,7] while maintaining a smaller bandgap in the absorber bulk. This reduces the interface recombination, as the hole barrier toward the buffer layer is increased.^[8]


1. Introduction

Sulfurization of Cu(In,Ga)Se_2 (CIGSe) absorber layers has been studied for many years^[1,2] and was used in the recent world record Cu(In,Ga)(S,Se)_2 (CIGSSe) solar cell of 23.35%.^[3] To improve CIGSe solar cells, an increasing $[\text{Ga}]/([\text{Ga}] + [\text{In}])$ (GGI) ratio toward the back contact and/or a decreasing $[\text{S}]/([\text{S}] + [\text{Se}])$ (SSSe) ratio from the surface to the bulk can be introduced. In both cases, the bandgap is gradually widened toward the corresponding interfaces, which reduces non-radiative

Other beneficial effects of the sulfurization were suggested as well: passivation of deep defect states,^[9,10] increase in hole mobility,^[11] and increase in electron lifetime.^[5] For the 23.35% world record and also by others,^[12–14] H_2S has been used for the sulfurization. In an attempt to avoid toxic H_2S , several studies were conducted on sulfurization of co-evaporated absorbers in elemental sulfur atmosphere,^[9,11,15,16] aiming at a similar device improvement. However, sulfurization in elemental S was found to induce the formation of a pure CuInS_2 (CIS) phase on top of the CIGSe (with a Ga accumulation at the CIGSe/CIS interface, which reduces the fill factor $[FF]$).^[17,18] Although the CIS layer introduces a higher surface bandgap and, consequently, has been observed to increase the open-circuit voltage,^[17] the conversion efficiency could not be improved, presumably due to the formation of an electron barrier at the CIGSe/CIS interface. For CuInSe_2 (CISE), it has been shown that sulfur diffusion is faster in Cu-rich compared with Cu-poor samples.^[19,20] A likely explanation is the rapid transformation of Cu_{2-x}Se precipitates within Cu-rich samples into $\text{Cu}_{2-x}(\text{S,Se})$, which then act as channels that accelerate sulfur in-diffusion and promote transformation of the absorber into a CuIn(S,Se)_2 alloy.^[21]

In this work, elemental sulfur incorporation into co-evaporated CIGSe and CuGaSe_2 (CGSe) absorber layers has been comparatively studied as a means to better understand the sulfurization of CIGSe absorber. To find the optimum conditions of S

F. Khavari, Dr. J. Keller, Dr. J. K. Larsen, Dr. K. V. Sopiha, Dr. T. Törndahl, Prof. M. Edoff
 Solar Cell Technology
 Department of Materials Science and Engineering
 Uppsala University
 Box 534, SE-75121 Uppsala, Sweden
 E-mail: Faraz.khavari@angstrom.uu.se

 The ORCID identification number(s) for the author(s) of this article can be found under <https://doi.org/10.1002/pssa.202000415>.

© 2020 The Authors. Published by Wiley-VCH GmbH. This is an open access article under the terms of the Creative Commons Attribution License, which permits use, distribution and reproduction in any medium, provided the original work is properly cited.

DOI: 10.1002/pssa.202000415

incorporation, the annealing temperature was varied from 330 to 530 °C. In this way, the resulting material quality and cell parameters could be compared across a range of annealing conditions, which allows to account for possible differences in sulfurization rates. In addition, the [Cu]/[III] ratio of the CGSe was varied from 0.55 to 1.14, which is meant to gain a deeper insight into the sulfurization and deduce the effect of off-stoichiometry.

2. Experimental Section

2.1. Film and Device Fabrication

Full stacks of thin-film solar cells based on p-type ternary chalcopyrite CISE or CGSe absorber layers were processed, as shown in Figure 1.

First, as the back contact, 350 nm of Mo was deposited on a 2 mm thick soda-lime glass (SLG) substrate using direct current-magnetron sputtering. In the next step, 15 nm of sodium fluoride (NaF) was deposited by thermal evaporation using an effusion source. Next, while the substrate temperature was ramping from 350 to 550 °C, the absorber layer of either CISE or CGSe was co-evaporated in a high vacuum deposition system. Flat evaporation rates were used for selenium and group-III elements, respectively, whereas the Cu rate followed a low rate–high rate–low rate protocol to implement the optimum three-stage-process profile. We used mass spectrometer control for the metal rates and temperature control for the selenium source. The composition was adjusted to $[Cu]/[III] = 0.86$ (where III is either Ga or In), unless otherwise specified. The composition values were extracted from X-ray fluorescence (XRF) measurements using a CIGSe standard sample with known composition. The thicknesses of the absorber layers were in the range of 1.5–1.9 μm ,

as estimated with XRF. Subsequently, the samples were divided into two equal pieces: one for sulfurization (see next paragraph) and another one as a reference. To protect the samples from oxidation, a cadmium sulfide (CdS) capping layer was grown by chemical bath deposition (CBD) within 5 min after removing the samples from the CIGSe evaporation system.

2.2. Sulfurization

Prior to the sulfurization, the capping layer of CdS was removed by etching in a solution of 2 M HCl for 60 s. The etched sample was immediately transferred into a custom-built furnace in a small graphite carrier box. After the sample was placed, 350 mg of elemental S was introduced into a preheated sublimation source chamber. Then, during 60 s, with a flow of argon (Ar) carrier gas, the vaporized sulfur was brought into the reactor at the estimated sample temperature $T_s = 330\text{--}530\text{ °C}$ (corresponding sample labeling is: CISE/CGSe- T_s). The Ar background pressure was set to 500 mbar. The sulfurization lasted for 10 min and was followed by cooling down in Ar atmosphere until room temperature was reached after about 30 min. More details about the sulfurization process and sulfurization system can be found in the previous study.^[17]

2.3. Solar Cell Fabrication

To create a pn junction, a $\approx 50\text{ nm}$ CdS buffer layer was deposited on top of the absorber layer using CBD. Then, a bilayer of 100 nm intrinsic ZnO (i-ZnO) and 230 nm aluminum-doped ZnO (ZnO:Al) was deposited by radio frequency magnetron sputtering. A metallic Ni/Al/Ni electrode was deposited through a shadow mask by electron-beam evaporation. Finally, mechanical

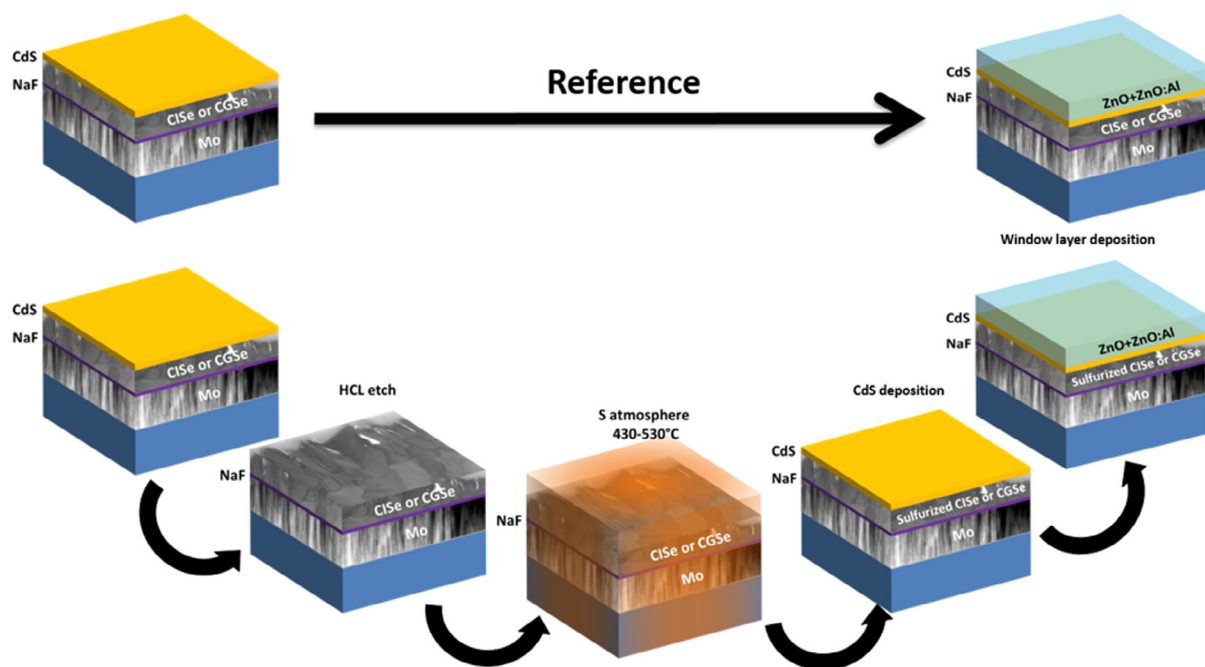


Figure 1. Schematic of a full stack processing of CISE and CGSe solar cell. Each sample is divided into two pieces: one for sulfurization (bottom) and one as a reference (top). CdS is removed before sulfurization and re-deposited again promptly after it. Identical window layers are deposited on both pieces.

scribing with a stylus was used to define individual solar cells with an area of 0.5 cm^2 . In this way, 12 cells were defined for each sample, which allowed to verify the lateral homogeneity and perform statistical analysis of the electrical characteristics.

2.4. Material and Electrical Characterization

Raman spectroscopy and X-ray diffraction (XRD) techniques were used to determine sulfur incorporation and crystallinity, respectively. The Raman excitation source was a 532 nm laser in a RENISHAW spectroscopy system. Both θ - 2θ and grazing incidence-XRD (GI-XRD) scans were conducted in a Philips X'pert MRDII system. Further cross-sectional imaging and elemental mapping were obtained by transmission electron microscopy and energy dispersive X-ray spectroscopy (TEM-EDS); FEI-Titan Themis 200, which operated at an acceleration voltage of 200 kV, where the TEM lamellae were prepared using focused ion beam. For investigation of compositional depth profiles, glow discharge optical emission spectroscopy (GDOES; Spectruma-Analytik-GMBH GDA 750) was performed. Finally, electrical characterization of solar cell devices was conducted using two homebuilt measurement setups: 1) current-voltage (J - V) under a Halogen lamp-solar simulator calibrated to AM 1.5G with an intensity of 100 mW cm^{-2} and 2) external quantum efficiency (EQE) under a Xe arc lamp.

2.5. Theory Method

The first-principles calculations were carried out within density functional theory using the Vienna Ab initio Simulation Package (VASP).^[22–24] The projector augmented wave (PAW) pseudopotentials^[25,26] with valence electron configurations of Cu $3d^{10}4s^1$, In $4d^{10}5s^25p^1$, Ga $3d^{10}4s^24p^1$, Se $4s^24p^4$, and S $3s^23p^4$ were used. The Perdew–Burke–Ernzerhof (PBE) exchange–correlation functional^[27] was utilized. The interaction parameters for enthalpies of Cu(III)(S,Se)₂ alloys were extracted from parabolic fits of 11 formation energy datapoints computed for the supercells containing 240 atoms (see Figure S1, Supporting Information). The stochastic nature of the alloys was reproduced with special quasi-random structure (SQS) algorithm^[28] implemented in the

Alloy-Theoretic Automated Toolkit (ATAT) package.^[29] Other example of such methodology applied to solar absorber alloys can be found in our earlier works.^[30,31] The Brillouin-zone integrations were performed using $3 \times 2 \times 2$ Γ -centered Monkhorst–Pack grid^[32] and a cutoff energy of 350 eV. The ionic force threshold for atomic relaxations was set to 0.01 eV \AA^{-1} . The lattice optimizations were allowed for all systems. To account for supercell errors, the formation energies of the terminal phases were adjusted to the corresponding values for the primitive cells of ternary chalcopyrites computed using a cutoff energy of 550 eV and k -points grids with a density of 4000 k -points per reciprocal atom.

3. Results and Discussion

This section is separated into three parts. First, a comparative material characterization of sulfurized CISE and CGSe with $[\text{Cu}]/[\text{III}] = 0.86$ is shown and discussed with the help of the first-principles calculations. In the second part, the impact of Cu content on sulfur incorporation into CGSe is presented. Finally, the corresponding solar cell characteristics are presented and discussed in the third part.

3.1. Materials Characterization: Comparison of CISE and CGSe

In this section, for a detailed analysis, we use a set of four complementary characterization techniques. In particular, we utilize Raman spectroscopy to detect sulfur in the near-surface regions, XRD to determine crystal structures of the formed phases, GDOES to evaluate depth profiles for the changes, and TEM-EDS to further examine surfaces locally and in detail.

3.1.1. Raman Spectroscopy

Figure 2 shows the Raman spectra of the CISE and CGSe samples before and after sulfurization at different temperatures. As shown in Figure 2a, the CISE samples exhibit the dominating peaks at 174 and 290 cm^{-1} . These two peaks are associated with the A_1 mode of Se–Se and S–S vibrations, respectively.^[33,34]

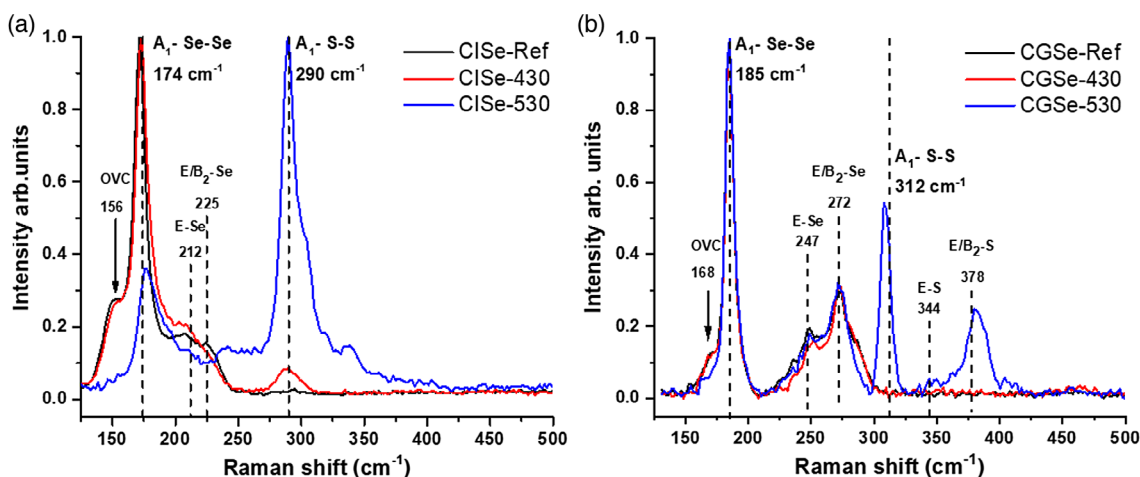


Figure 2. Normalized peak intensities of Raman spectra of a) CISE and b) CGSe thin films sulfurized at different temperatures.

Importantly, the A_1 -Se-Se peak intensity decreases, as the A_1 -S-S peak becomes more pronounced with sulfurization temperature, which is a direct evidence of sulfur incorporation within the probing depth of the Raman laser (about 200 nm^[35]). In addition, the A_1 -Se-Se peak shifts toward higher wavenumbers and broadens for both sulfurized samples, which indicates the formation of a $\text{CuIn}(\text{S},\text{Se})_2$ alloy. The full width half maximum (FWHM) values of the aforementioned peaks increase from 12.9 cm⁻¹ for the CISE-Ref sample to 14.5 and 29.0 cm⁻¹ for the CISE-430 and CISE-530 samples, respectively. No noticeable shift or broadening was observed for the second peak at 290 cm⁻¹. This is in agreement with the behavior previously described for $\text{CuIn}(\text{S},\text{Se})_2$ alloys.^[33]

In contrast to the CISE-430 sample, no sulfur peaks can be distinguished in Raman spectra for the CGSe-430 sample, suggesting a negligible amount of incorporated sulfur. However, sulfur was certainly introduced into the CGSe-530 sample, because the sulfur peaks corresponding to A_1 , E, and E/B_2 modes of S-S vibrations appear around 312, 344, and 378 cm⁻¹, respectively (Figure 2b). At the same time, no broadening or shift of the A_1 -Se-Se peak is observed for this sample. Further investigations are needed to verify if pristine CuGaS_2 (CGS) crystals or a $\text{CuGa}(\text{S},\text{Se})_2$ alloy is formed.

The peaks at 156 and 168 cm⁻¹ indicate CuIn_3Se_5 and CuGa_3Se_5 ordered vacancy compounds (OVC), respectively. These phases are clearly present at the surfaces of the references and both samples sulfurized at 430 °C. The peak intensities decrease after sulfurization at 530 °C for both compounds, probably due to the formation of closed surface layers covering the OVC.

3.1.2. X-Ray Diffraction

Figure 3 shows the results of the XRD analysis for the CISE-430 and CISE-530 samples. For both sulfurized samples in Figure 3a, the (112) peak at 26.6° is slightly broadened asymmetrically to higher 2 θ angles, which points to S incorporation in the form of an alloy. Furthermore, for CISE-530, a second peak emerges at $\approx 27.8^\circ$, which corresponds to the (112) peak of CIS (JCPDS No.01-075-0106).^[36] It should be noted that this new peak is very close to the (103) peak of CISE at 27.65°, meaning that these signals can overlap. As such, to amplify the signal from the near-surface regions, the GI-XRD analysis at a grazing incidence angle $\alpha = 0.5^\circ$ was carried out. As shown in Figure 3b, a clear tail appears already in CISE-430, and it evolves into a distinct peak in CISE-530. This strong dependence on the sulfurization

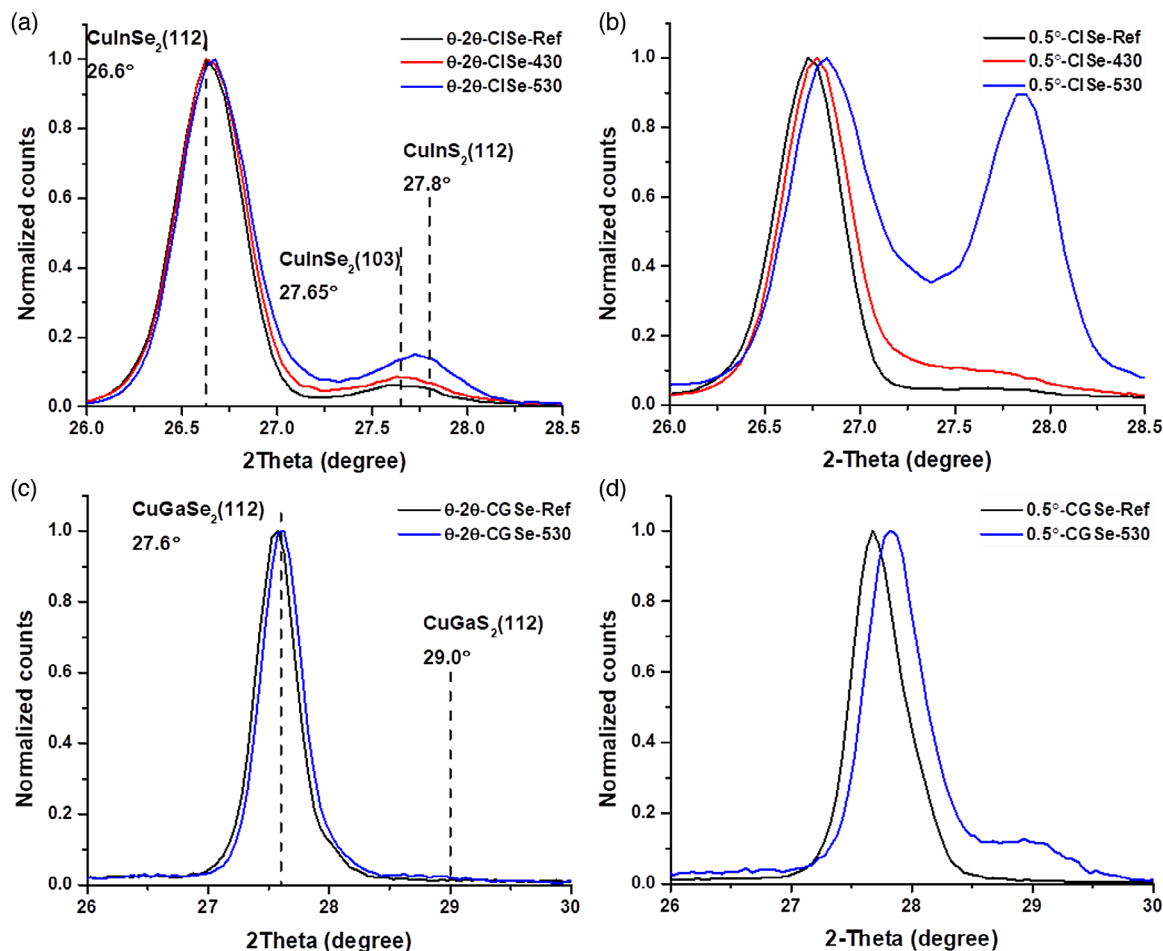


Figure 3. XRD analysis of sulfurized a,b) CISE and c,d) CGSe samples. a,c) θ -2 θ scans and b,d) GI-XRD scans at $\alpha = 0.5^\circ$. CGSe-430 was not analyzed by XRD, because no sulfur was detected by Raman.

temperature indicates the presence of CIS crystals at least for CISE-530. Moreover, there is a systematic shift in the CISE (112) peak position, which implies that the $\text{CuIn}(\text{S,Se})_2$ alloy forms in the surface region at temperatures as low as 430 °C.

For the CGSe-530 sample, a peak shift to higher 2θ angles is seen directly from θ - 2θ scans in Figure 3c, which indicates the $\text{CuGa}(\text{S,Se})_2$ formation. Furthermore, as shown with GI-XRD in Figure 3d, not only the (112) peak shifts, but also a secondary peak emerges at the position of CGS.^[37] We interpret these changes as the formation of CGS and $\text{CuGa}(\text{S,Se})_2$ phase mixture close to the surface of the sample sulfurized at 530 °C.

3.1.3. GDOES Profiling

Figure 4 shows the semi-logarithmic GDOES profile for the CISE and CGSe stacks. The interfaces are defined by the onset of the sulfur and copper signals. After the sulfurization of both films, the Se concentration decreases, as the S content increases below the CdS buffer. Importantly, the graphs show deeper and more significant S incorporation in CISE, in good agreement with the GI-XRD analysis. Negligible S concentration is measured at the Mo back contact (not shown here), indicating that the sulfurization did not chemically alter the MoSe_2 layer, which is usually formed during absorber deposition.^[38,39] Moreover, the GDOES results indicate a slight enrichment in Cu near the buffer in CISE-530 but not for CGSe-530.

3.1.4. TEM-EDS Imaging

The TEM-EDS analysis of CISE-430, CISE-530, and CGSe-530 samples is shown in Figure 5. For the CISE-430 sample, S is predominantly incorporated at the surface and in grain boundaries/cavities. There is no closed CIS layer visible for this sample within the resolution limit of TEM-EDS (in the order of 5 nm). For the CISE-530, a fully covering layer of CIS with varying thickness is observed. For both CISE samples, a consistent increase in Cu concentration is evident in all regions of noticeable S incorporation (see Figure S2, Supporting Information). This behavior is likely to originate from the $\text{CuIn}(\text{S,Se})_2$ formation requiring

near-stoichiometry of $[\text{Cu}]/[\text{III}] \approx 1$,^[40] which stimulates Cu diffusion toward the reaction front during sulfurization. As a result, the rate of Cu supply may become the limiting factor for S incorporation into CISE as observed previously in our group.^[21] For the CGSe-530, sulfur enrichment was found at the surface with no evidence of a closed CGS layer. Instead, widely dispersed of what appears to be small CGS particles were found, which explains the corresponding signature in GI-XRD for this sample. In contrast to CISE, there does not seem to be a Cu increase in the regions of S incorporation (see Figure S2, Supporting Information). This indicates that the sulfurization of CGSe does not incur as much Cu diffusion toward the reaction front as is the case for CISE.^[21] In other words, CGSe surface remains Cu-deficient even after the S incorporation, signifying that Cu-supply controlled mechanisms do not apply to CGSe. Furthermore, accounting for the similarities in lattice structures of CGSe and CISE, this finding points to the need to revisit the hypothesis about the governing role of Cu supply in sulfurization of CISE.

3.1.5. First-Principles Calculations

By comparing CISE-430 and CGSe-530, we can estimate that CGSe needs roughly 100 °C higher temperature to reach a similar level of S incorporation. Fundamentally, there are only two possibilities why this could be the case; it is either 1) more favorable *thermodynamics* or 2) faster *kinetics* of the underlying processes for CISE. To test the former scenario, one can compare energies for converting CISE and CGSe into the sulfides. Unfortunately, to the best of our knowledge, standard enthalpy of formation of CGS has not been reported, whereas the values for CIS and CISE^[41] seem inconsistent with model estimations.^[42] Therefore, as an approximation, we obtained all enthalpies of formation (ΔH_f) from the first-principles calculations. The computed values of ΔH_f for CISE, CGSe, CIS, and CGS are -1.7819 , -1.9287 , -1.9728 , and -2.3282 eV formula⁻¹, respectively. We did not implement any correction of chemical potentials for elemental solids, because they anyway cancel out in the calculation of reaction energies below. In fact, the same conclusions were obtained with two different correction schemes implemented in the Materials Project^[43] and Open Quantum

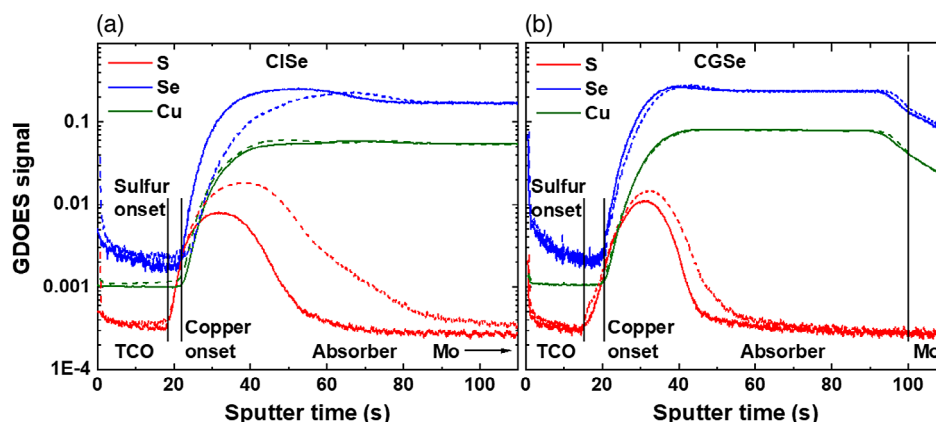


Figure 4. GDOES profiles of a) CISE and b) CGSe stacks. The solid and dashed lines represent reference and sulfurized (at 530 °C) samples, respectively. The sulfur signals in the reference samples emanate from the CdS buffer layers. For a better visualization, the curves are aligned with respect to the onset of the S signal of the CdS buffer.

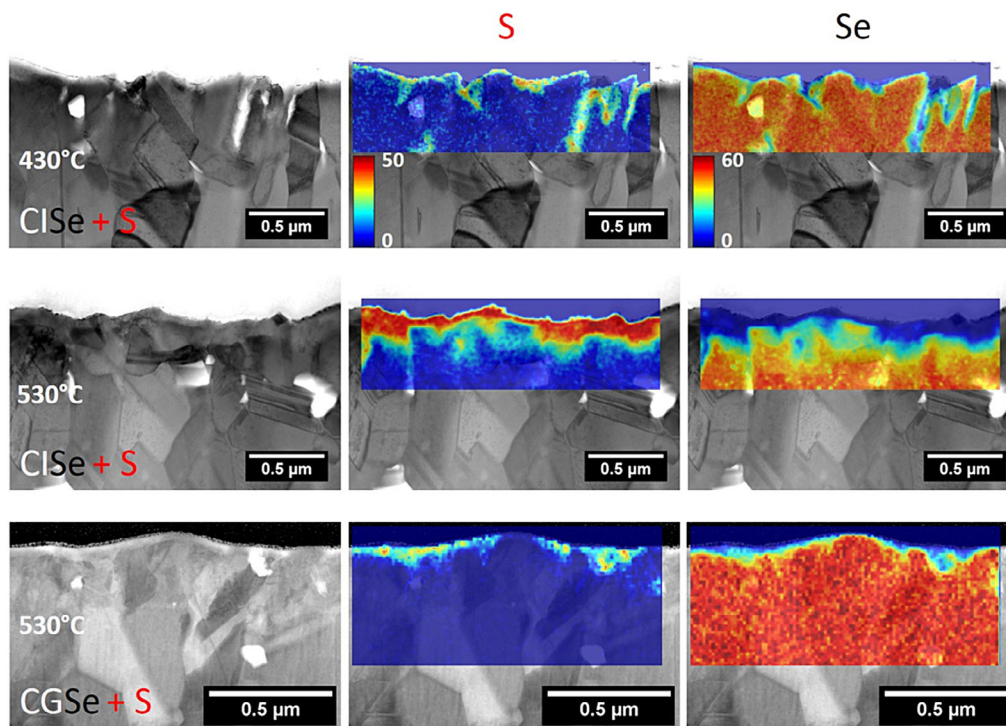
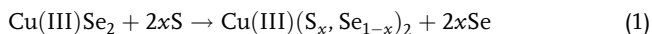


Figure 5. TEM-EDS cross-sectional imaging of ClSe-430 (top), ClSe-530 (middle), and CGSe-530 (bottom) films. The scales of color bars in the middle and right columns quantify at% of S and Se, respectively.

Materials Database (OQMD).^[44] Next, we extracted the interaction parameters (Ω) for $\text{CuIn}(\text{S,Se})_2$ and $\text{CuGa}(\text{S,Se})_2$ from the parabolic fits of formation energies for random alloy supercells (see the Experimental Section) and obtained 78.5 and 130.4 meV formula⁻¹, respectively, where the former agrees well with a previous report by Chen et al.^[45] Using the regular solution model, these values translate into the consolute temperatures of -45 and 106°C for the respective systems, meaning that both of them are completely miscible at the used sulfurization temperatures. This is not surprising as there are multiple reports of successful synthesis of CIGSs alloys with arbitrary compositions.^[7] The larger interaction parameter for $\text{CuGa}(\text{S,Se})_2$ could lead to slower intermixing between CGSe and CGS from a diffusion couple. However, for the used sulfurization by annealing in S-rich atmosphere, the process is better described by enthalpies (ΔH_f) of the following reactions



The computed values of ΔH_f for (III) = In and Ga are $-190.9 \cdot x + 78.5 \cdot x(1-x)$ and $-399.5 \cdot x + 130.4 \cdot x(1-x)$ meV formula⁻¹, where $x \equiv \text{SSe}$ (see Figure S1, Supporting Information), respectively, indicating that CGSe is thermodynamically more favorable to sulfurize at all SSe values. This conclusion clearly contradicts our experimental findings, thereby pointing to the dominance of kinetic factors, most likely slower diffusion of S in bulk CGSe compared with ClSe. This could be justified by more densely packed lattice of CGSe (smaller ionic radius of Ga), which may impede S diffusion by increasing both the

migration barrier and formation energy of S interstitials. Unfortunately, complexity of diffusion pathways in defective chalcopyrite restrains further computational verification of this trend. It is possible to conclude, however, that S incorporation into CGSe is limited by slower S in-diffusion and not by the thermodynamic factors.

3.2. Sulfurized CGSe with Varying Cu Content

To investigate the influence of Cu off-stoichiometry on sulfurization of CGSe, a series of samples with different $[\text{Cu}]/[\text{III}]$ ratios were fabricated, and their sulfurization was compared in this section.

3.2.1. Raman Spectroscopy

Figure 6 shows the Raman spectra of CGSe samples with $[\text{Cu}]/[\text{III}]$ varying from 0.55 (very Cu-poor) to 1.14 (Cu-rich), before and after sulfurization. Raman peaks at 168 cm^{-1} indicate the presence of OVC for the two Cu-poor samples in Figure 6a,b. We find that the appearance of sulfur peaks correlates with a decrease in intensity of the OVC peak, indicating that the OVC is buried under a layer formed at the surface. Moreover, we get more S incorporated into the sample with a $[\text{Cu}]/[\text{III}]$ of 0.55 than 0.86, akin to the behavior of ClSe observed in our previous study.^[21] As expected, the near-stoichiometric ($[\text{Cu}]/[\text{III}] = 0.95$) and Cu-rich ($[\text{Cu}]/[\text{III}] = 1.14$) samples show no evidence of OVC neither before nor after the sulfurization.

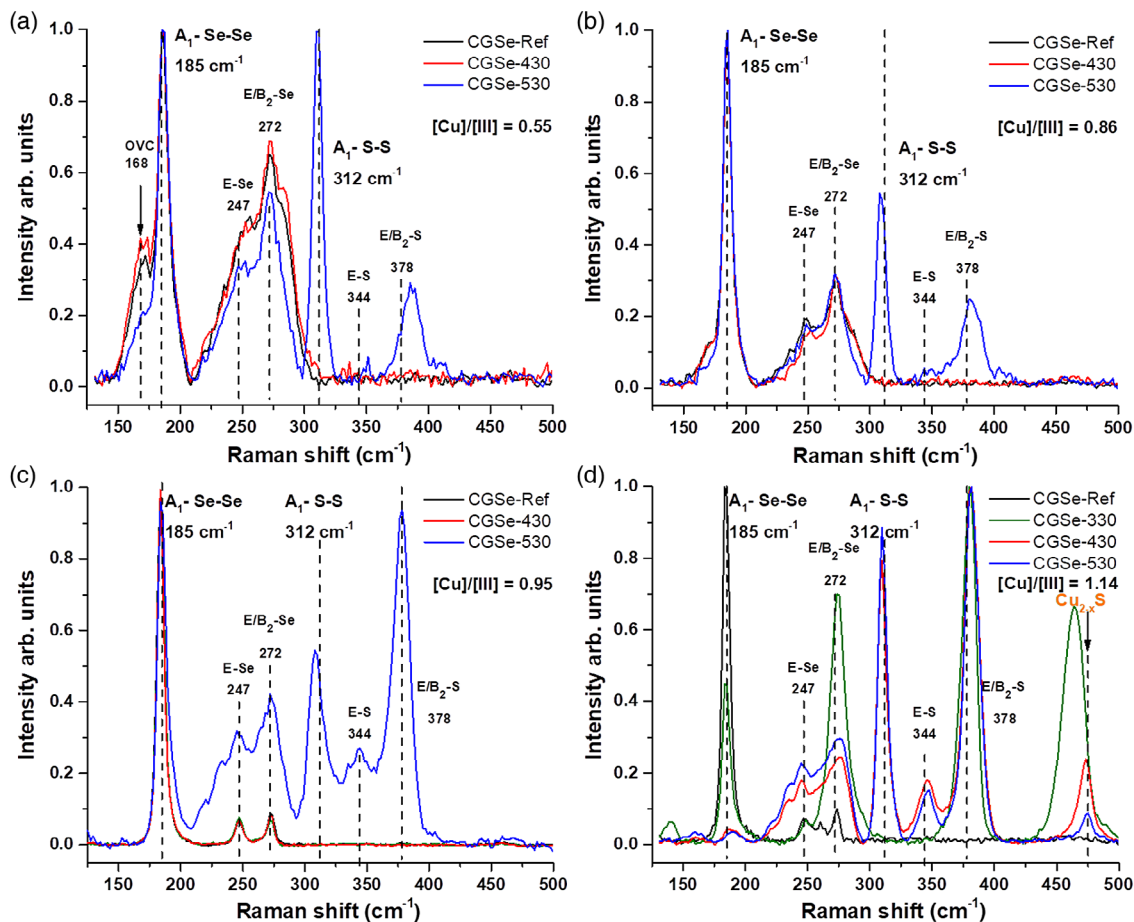


Figure 6. Normalized Raman spectra for CGSe thin films with a) $[Cu]/[III] = 0.55$, b) $[Cu]/[III] = 0.86$, c) $[Cu]/[III] = 0.95$, and d) $[Cu]/[III] = 1.14$ sulfurized at different temperatures.

For the Cu-poor and near-stoichiometric samples, sulfur incorporation is only significant at 530 °C, as can be concluded from the appearance of the corresponding A_1 -S-S signature. The behavior of the Cu-rich sample ($[Cu]/[III] = 1.14$) is drastically different. Here, a large amount of S is incorporated already at 330 °C but as $Cu_{2-x}(S,Se)$, as is evident from the appearance of intense Raman peaks at 272 and 460 cm^{-1} (green line in Figure 6d).^[46] At the higher sulfurization temperatures of 430 and 530 °C, these peak intensities decrease, whereas the latter peak position shifts toward that of $Cu_{2-x}S$ at 475 cm^{-1} .^[46] Moreover, the peak corresponding to the A_1 -S-S vibrational mode of CGS emerges already at 430 °C (red line in Figure 6d), suggesting that the presence of $Cu_{2-x}(S,Se)$ in the Cu-rich films promotes sulfurization of CGSe. A likely scenario is that residuals of $Cu_{2-x}Se$ secondary phase in the grain boundaries undergo rapid transformation into $Cu_{2-x}(S,Se)$ and subsequently into $Cu_{2-x}S$ upon exposure to S-rich atmosphere, and then act as the channels supplying S into the film interior. As such, the slow kinetics of S incorporation into the chalcopyrite phase stops being the limiting factor for sulfurization, resulting in much faster conversion of Cu-rich CGSe into CGS. Further investigation by TEM-EDS was made to verify this hypothesis.

3.2.2. TEM-EDS Imaging

The heterogeneous character of S incorporation is best exemplified by the TEM-EDS analysis of near-stoichiometric CGSe with $[Cu]/[III] = 0.95$ in Figure 7. In the reference sample, the surface region contains grains of the $Cu_{2-x}Se$ phase (encompassed by black circles). This is not surprising, considering that $Cu_{2-x}Se$ and $Cu_{2-x}S$ tend to segregate in Cu-rich films^[47–49] and are often detected in Cu-poor absorbers as residuals from the three-stage deposition.^[50] After the sulfurization, these $Cu_{2-x}Se$ inclusions are converted into $Cu_{2-x}S$ (or $Cu_{2-x}(S,Se)$ with minor Se concentration; shown by the white arrows), whereas the CGSe grains are barely affected. Importantly, small patches of $CuGa(S,Se)_2$ alloy can be distinguished at the left edge of the $Cu_{2-x}S$ inclusion pointed to by the arrows to the right in each image, confirming the catalyzing role played by $Cu_{2-x}(S,Se)$ in S incorporation and proving limited S diffusion into bulk CGSe. A weak S signal (≈ 3 at%) anti-correlating with the Se distribution is traceable along the grain boundaries. This can be explained by $Cu_{2-x}Se$ residuals in grain boundaries transforming into $Cu_{2-x}(S,Se)$ during the sulfurization. Although not resolved with TEM-EDS, this phase could convert the grain boundaries

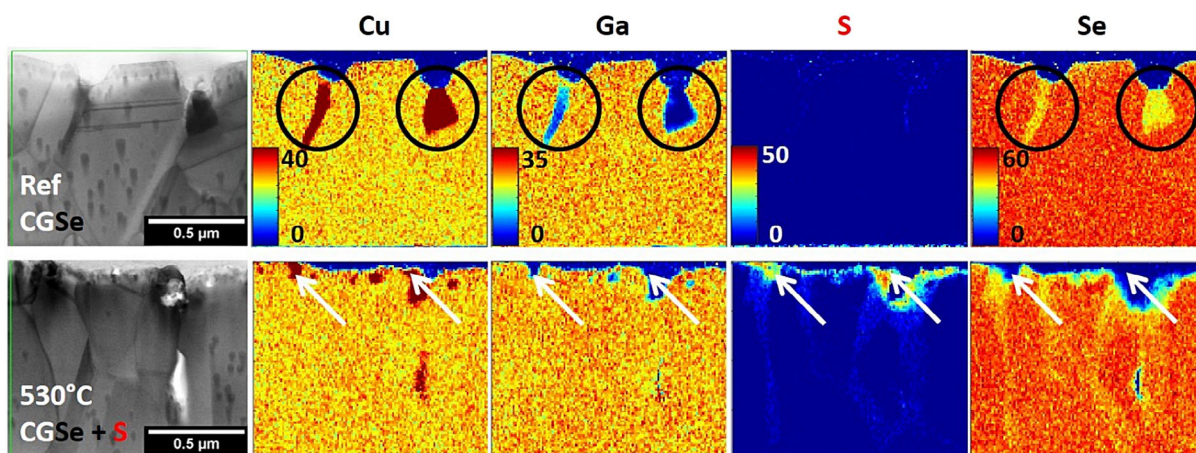


Figure 7. TEM-EDS cross-sectional analysis of CGSe-Ref (top) and CGSe-530 (bottom) films with $[\text{Cu}]/[\text{III}] = 0.95$.

into the rapid S diffusion channels, thereby facilitating sulfurization of the entire film. This reaction path should be responsible for the rapid sulfurization of the Cu-rich CGSe ($[\text{Cu}]/[\text{III}] = 1.14$), as we hypothesized based on Raman spectra described earlier. It cannot be ruled out, however, that a part of the explanation is the inherently higher diffusion in grain boundaries, which may themselves transport S at higher rates compared with bulk CGSe.

3.3. Solar Cell Performance

Solar cells were made from the samples with $[\text{Cu}]/[\text{III}] = 0.86$ to investigate the influence of sulfurization on device performance. Although special care was taken to protect the surfaces from unwanted reactions such as oxidation, all sulfurized sample still had to go through several extra process steps involving short air exposures, which could have an adverse effect on the cell quality. The general tendencies could still be deduced, and the main cell results are presented as follows.

3.3.1. Properties of CISE Devices

The results from J - V measurements on the CISE samples are summarized in **Figure 8**. The solar cells were made from different regions of the same samples and characterized using the Raman, XRD, GDOES, and TEM-EDS, details of which are discussed in the previous sections.

Statistical variations of the electrical characteristics for sulfurized and reference CISE cells are given in **Figure 8**. The EQE and J - V measured for devices with the highest V_{oc} values are presented in **Figure 9**. From the J - V curves in **Figure 9b**, the extracted series resistance values (extracted from the J - V curves as the reciprocal slope at $V = V_{\text{oc}}$) increase from $1.49 \Omega \text{ cm}^2$ for the CISE-Ref sample to 1.51 and $2.24 \Omega \text{ cm}^2$ for the CISE-430 and CISE-530 samples, respectively. The highest efficiency is obtained for the CISE-430 sample. Here, we observe an improvement in V_{oc} ($\approx 60 \text{ mV}$) and a slight increase in FF ($\approx 2\%$) compared with the non-sulfurized reference sample. However, the

EQE analysis indicates slightly lower collection for $\lambda > 700 \text{ nm}$, which signifies increased losses for electrons generated further away from the heterojunction. As a result, the J_{sc} is slightly decreased after the sulfurization at 430°C for the sample shown in **Figure 9**, although this cannot be stated as a general trend, because the changes in current are within the standard deviation (error bar). For the sample annealed at 530°C , a severe deterioration of all device parameters is observed. At the same time, the EQE analysis suggests that the effective optical bandgap remains unchanged, which is reasonable, because the S-containing surface is expected to have a wider gap compared with the main absorbing CISE layer underneath.

To further explore the origin of the collection losses (drop in EQE), we performed EQE measurements at an applied bias of -0.5 V on the sulfurized samples and compared them with the EQE spectra at short circuit condition. The results are shown in **Figure 10**.

The CISE-430 sample shows only a marginally improved collection (i.e., widening of space charge region has only minor effect), indicating negligible electrical J_{sc} changes after the low temperature sulfurization. In contrast, the CISE-530 sample shows a significantly increased EQE with negative voltage bias, approaching the EQE level of the CISE-430 sample. **Figure 10c** shows the ratios of the biased EQE to non-biased measurements for the corresponding samples. While the slight gain for the CISE-430 sample is found for the longer wavelengths, the CISE-530 sample shows continuously improving carrier collection with increasing wavelength for $\lambda > 400 \text{ nm}$. This points to a reduced diffusion length after sulfurization at 530°C . Possible reasons may be the creation of deep S-related point defects in the absorber bulk or altered electrical properties of grain boundaries (e.g., by Cu enrichment). In addition to the increasing collection with wavelength, a step-like increase at $\approx 810 \text{ nm}$ is visible, which corresponds to the absorption edge (bandgap energy) of the newly formed CIS top layer. This indicates the existence of a transport barrier at the CISE/CIS contributing to the collection losses. From the TEM analysis (not shown here), it is found that the extension of the CIS region into the absorber varies locally

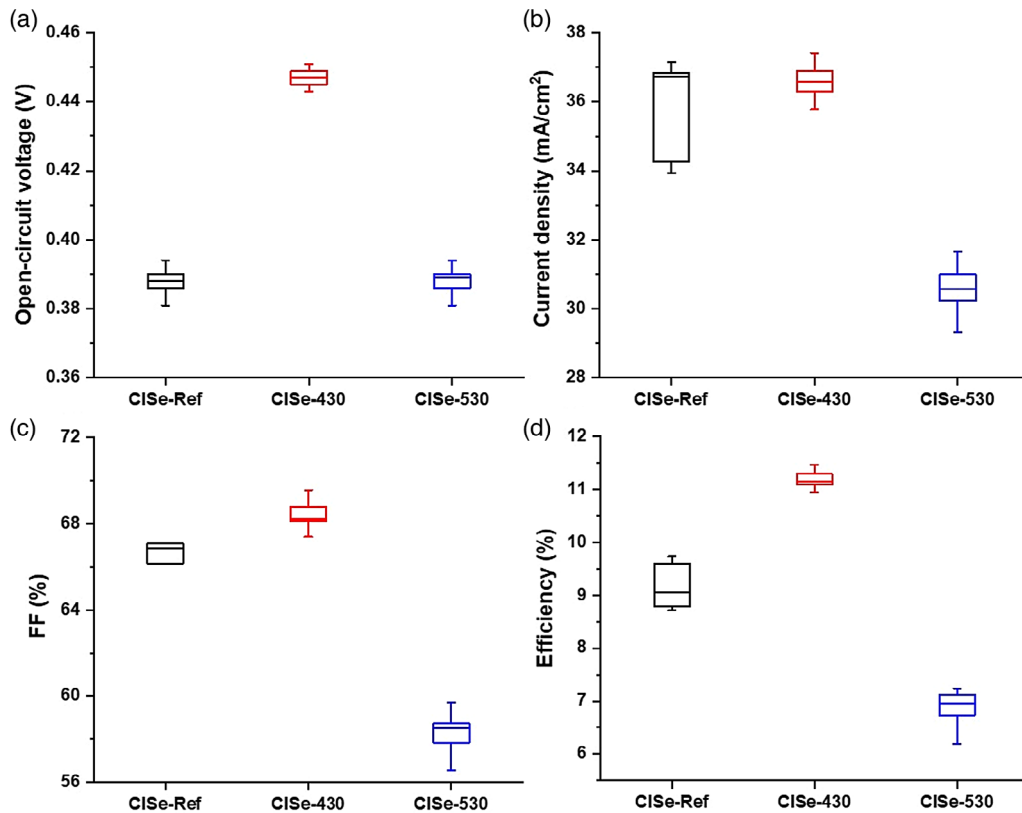


Figure 8. Solar cell parameters of a) V_{oc} (V), b) J_{sc} (mA cm^{-2}), c) FF (%), and d) efficiency (%) are compared for the sulfurized and reference CISE devices with $[\text{Cu}]/[\text{III}] = 0.86$ as extracted from J - V measurements.

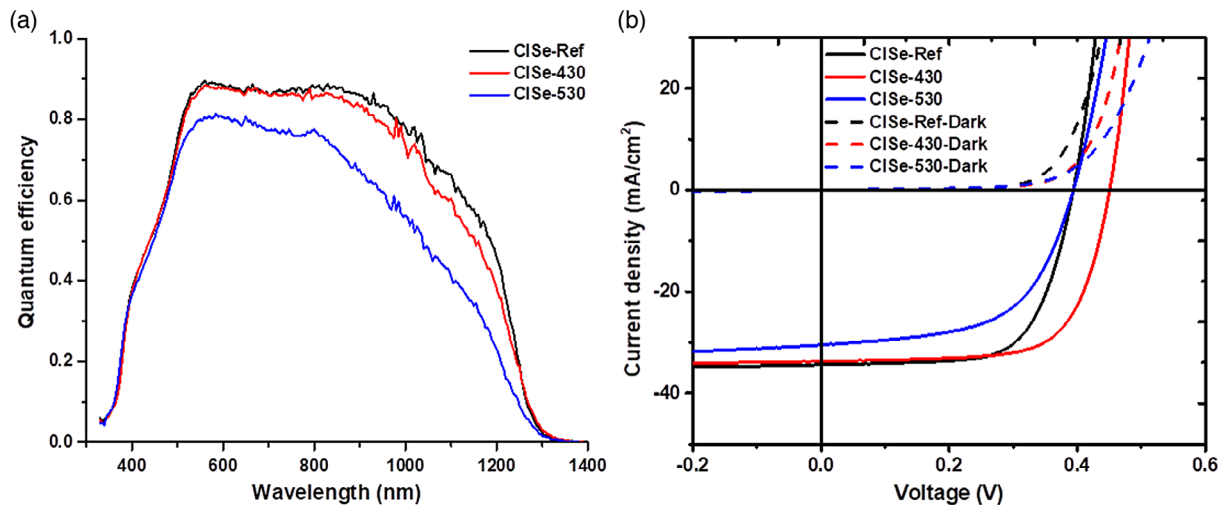


Figure 9. a) EQE and b) J - V for the sulfurized and reference CISE solar cells as measured on the devices with the highest V_{oc} values. The dark and light J - V are given by the dashed and solid lines, respectively.

between 50 and 180 nm for the CISE-530 sample. Thus, a voltage bias of -0.5 V may locally move the edge of the space-charge region across the CISE/CIS interface, thereby reducing the effective barrier height.

The findings explain the observed FF reduction after too strong sulfurization, which was not observed in the previous

study^[21] (i.e., for thinner CIS layers), thereby indicating that a transport barrier evolves at the CIS/CISE interface when the CIS layer becomes too thick. However, the complexity of the newly formed heterojunction does not allow to exclude other mechanisms affecting the carrier collection, such as increased recombination at either CISE/CIS or CIS/CdS interface.

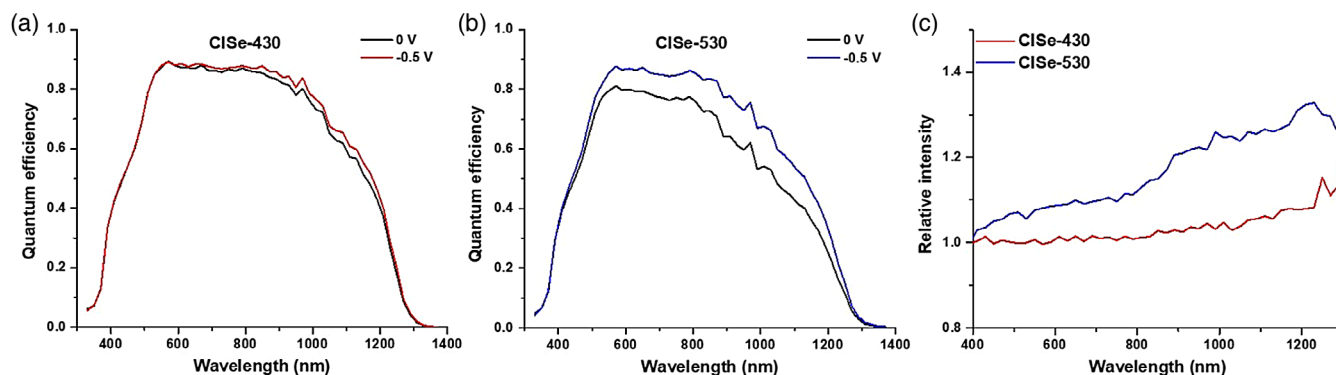


Figure 10. a,b) Bias-dependent EQE of the CISE-430 and CISE-530 devices. c) The ratios of biased and unbiased EQE are presented for clarity.

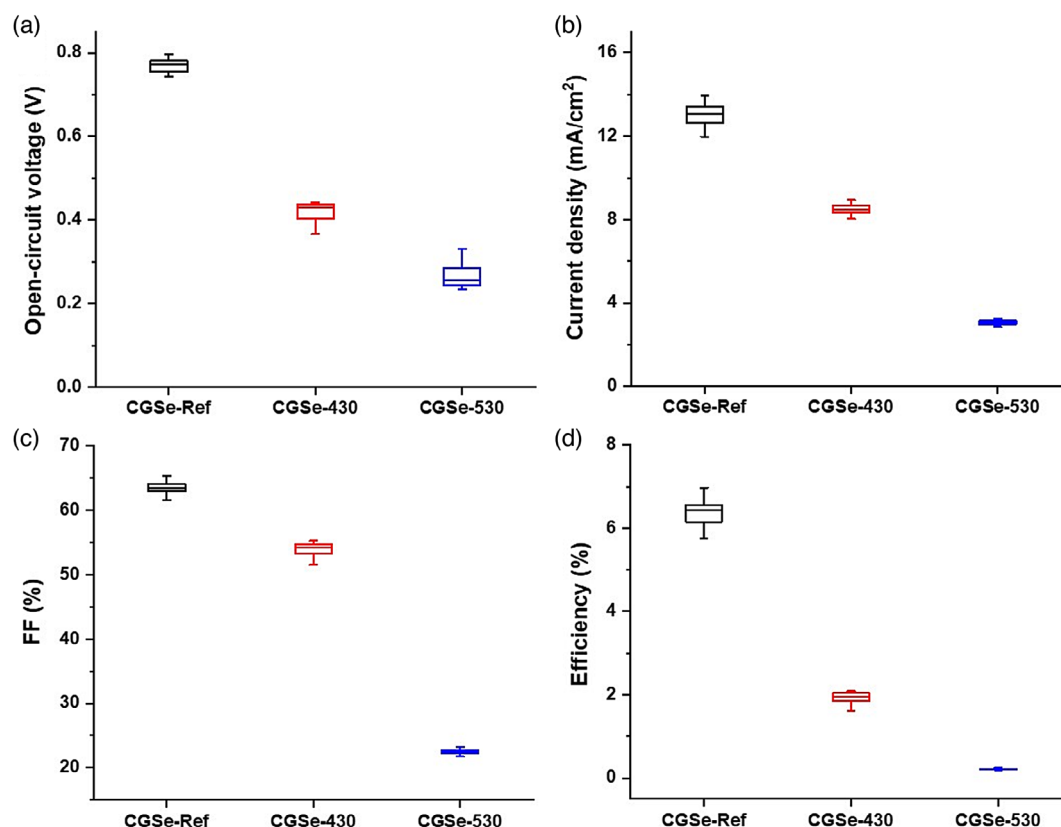


Figure 11. Solar cell parameters of a) V_{oc} (V), b) J_{sc} (mA cm^{-2}), c) FF (%), and d) efficiency (%) are compared for the sulfurized and reference CGSe devices with $[\text{Cu}]/[\text{III}] = 0.86$ as extracted from J - V measurements.

3.3.2. Properties of CGSe Devices

Figure 11 shows the J - V characteristics of the CGSe sample. In general, due to the wider bandgap of 1.68 eV for CGSe compared with 1.04 eV for CISE, higher V_{oc} and lower J_{sc} are expected for CGSe devices. Indeed, this trend is observed for the reference cells. However, in contrast to the improvements observed for CISE, V_{oc} drops significantly after the sulfurization of CGSe absorbers, with the deterioration being more severe for higher annealing temperature. Similarly, the EQE of the sulfurized

samples is reduced for all wavelengths (see **Figure 12**), which can be caused by a variety of factors. Severe degradation is particularly surprising for CGSe-430, which showed no signs of sulfur alloying in XRD and Raman spectra. As such, other factors related to S-based point defects or different Na distribution are likely responsible for this loss in performance. The negative trends are observed for J_{sc} and FF as well, thereby consolidating the overall adverse effect of sulfurization on CGSe devices.

Fundamentally interesting changes in electrical performance were observed for the Cu-rich CGSe ($[\text{Cu}]/[\text{III}] = 1.14$) devices.

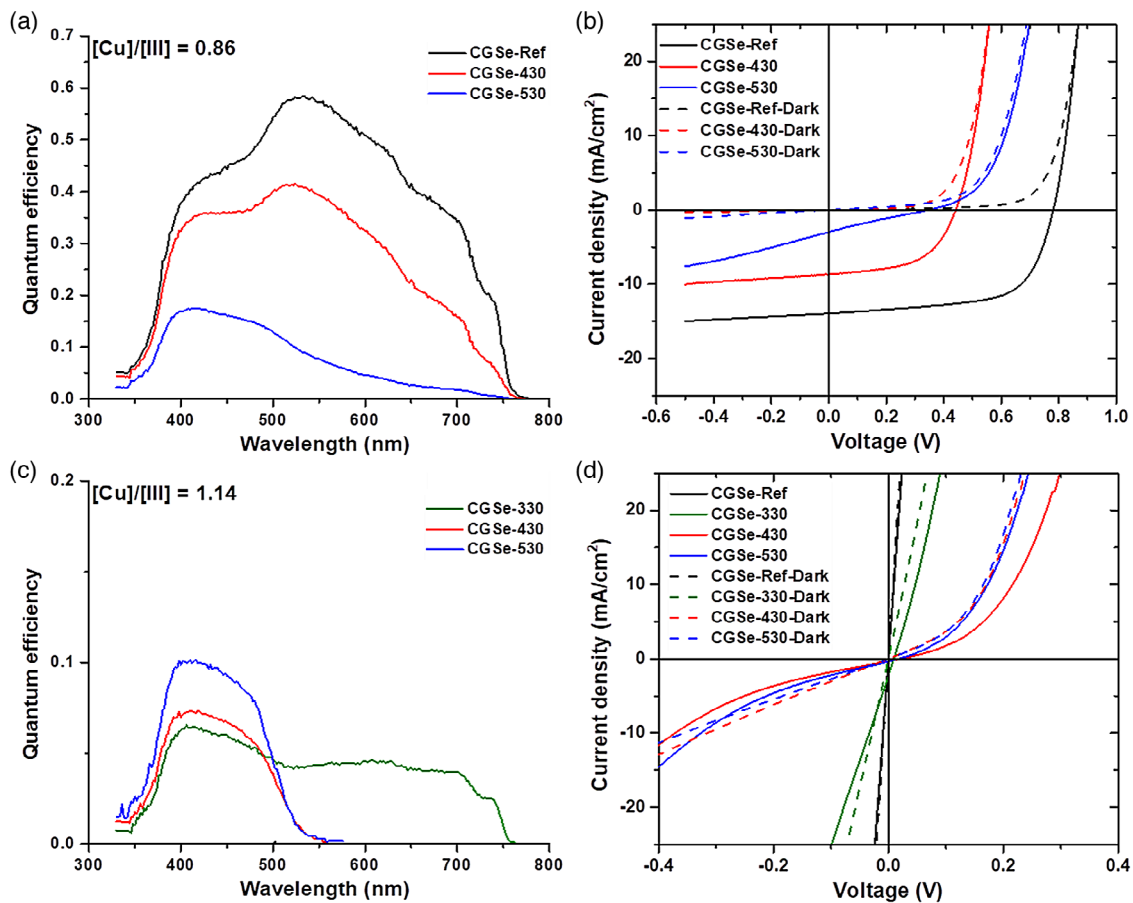


Figure 12. The corresponding a,c) EQE and b,d) J - V graphs of the CGSe sample with $[Cu]/[III] = 0.86$ and 1.14 , before and after sulfurization. The EQE of CGSe-Ref is not included in c), because it is zero for all wavelengths.

All cells made of these references were shunted due to the metallic conductivity of $Cu_{2-x}Se$ phase.^[51] However, they became weak diodes and started giving photovoltaic response after sulfurization at $330^{\circ}C$, as shown in Figure 12c,d. For higher annealing temperatures, the EQE at $\lambda < 500$ nm increased, absorption/collection at $\lambda > 500$ nm diminished, and the effective bandgap approached the corresponding value for CGS (2.4 eV). These transformations can be explained by the conversion of $Cu_{2-x}Se$ into $Cu_{2-x}S$, which is then followed by its complete consumption at higher temperatures. These results once again highlight the catalyzing role of $Cu_{2-x}Se$ in sulfurization of chalcopyrite absorbers.

4. Conclusion

In this work, sulfurization of CISE and CGSe in elemental sulfur atmosphere was performed at the temperatures ranging from 330 to $530^{\circ}C$. The resulting films were analyzed using Raman, XRD, GDOES, and TEM-EDS. We found several profound differences in sulfurization of Cu-poor CISE and CGSe. In particular, while surfaces of the CISE films accepted significant amounts of sulfur already at $430^{\circ}C$, the CGSe films required about $100^{\circ}C$ higher annealing temperature to achieve a similar level of

S incorporation. This tendency can be justified by slower diffusion of S in CGSe, as the thermodynamic factors point to the faster sulfurization of CGSe. However, Cu-rich CGSe films were found to incorporate large amounts of sulfur at a temperature as low as $330^{\circ}C$. We explain the facilitated sulfurization of these films by a two-step transformation of the segregated $Cu_{2-x}Se$ residuals via $Cu_{2-x}(S,Se)$ into CGS crystals. Another difference is that a fully covering CIS layer is formed at the CISE surface after sulfurization at $530^{\circ}C$. For CGSe, however, there was no evidence of a closed layer of CGS. Furthermore, CGS seemingly allows for a larger off-stoichiometry than CIS, which can only form at $[Cu]/[III] \approx 1$ and imposes similar constraints on the formation of $CuIn(S,Se)_2$. Thus, no long-range redistribution of Cu is necessary to form the $CuGa(S,Se)_2$ layer at the CGSe surface, suggesting that Cu diffusion is not the governing factor in sulfurization of chalcopyrites. On the device level, sulfurization of CGSe was found to have a strong adverse effect on all cell parameters, even when no significant S incorporation was taking place. This result is also in contrast with CISE cells, which showed a small improvement in V_{oc} and FF for the absorber sulfurized at $430^{\circ}C$, resulting in the overall 1.5% efficiency improvement for the best cell. However, for the CISE absorber sulfurized at $530^{\circ}C$, lower diffusion length accompanied by possible formation of an electron transport barrier can explain a decreasing FF and short-circuit current density (J_{sc}).

Supporting Information

Supporting Information is available from the Wiley Online Library or from the author.

Acknowledgements

This work was supported by the Swedish Foundation for Strategic Research (SSF) under the project number RMA15-0030. The authors would like to thank the access to high-performance computing resources provided by Swedish National Infrastructure for Computing (SNIC). They also acknowledge L. Riekehr for carrying out STEM-EDS analysis, as well as all the colleagues in the solar cell division at the Ångström laboratory for their help and valuable contributions.

Conflict of Interest

The authors declare no conflict of interest.

Keywords

diffusion, elemental sulfur, ordered vacancy compounds, phase transformation, sulfurization

Received: June 30, 2020

Revised: August 13, 2020

Published online: September 29, 2020

- [1] M. Marudachalam, H. Hichri, R. Klenk, R. W. Birkmire, W. N. Shafarman, J. M. Schultz, *Appl. Phys. Lett.* **1995**, 67, 3978.
- [2] M. A. Green, E. D. Dunlop, D. H. Levi, J. Hohl-Ebinger, M. Yoshita, A. W. Y. Ho-Baillie, *Prog. Photovolt. Res. Appl.* **2019**, 27, 565.
- [3] Solar Frontier press release, http://www.solar-frontier.com/eng/news/2019/0117_press.html (accessed: May 2019).
- [4] S. Wei, A. Zunger, *J. Appl. Phys.* **1995**, 78, 3846.
- [5] V. Probst, W. Stetter, W. Riedl, H. Vogt, M. Wendl, H. Calwer, S. Zweigart, K.-D. Ufert, B. Freienstein, H. Cerva, F. H. Karg, *Thin Solid Films* **2001**, 387, 262.
- [6] T. Kobayashi, H. Yamaguchi, Z. J. L. Kao, H. Sugimoto, T. Kato, H. Hakuma, T. Nakada, *Prog. Photovolt. Res. Appl.* **2015**, 23, 1367.
- [7] T. Maeda, R. Nakanishi, M. Yanagita, T. Wada, *Jpn. J. Appl. Phys.* **2020**, 59, SGGF12.
- [8] T. Kato, *Jpn. J. Appl. Phys.* **2017**, 56, 04CA02.
- [9] D. Ohashi, T. Nakada, A. Kunioka, *Sol. Energy Mater. Sol. Cells* **2001**, 67, 261.
- [10] R. Knecht, M. S. Hammer, J. Parisi, I. Riedel, *Phys. Status Solidi A* **2013**, 210, 1392.
- [11] M. Beres, K. M. Yu, J. Syzdek, S. S. Mao, *Thin Solid Films* **2016**, 608, 50.
- [12] R. Kamada, T. Yagioka, S. Adachi, A. Handa, K. F. Tai, T. Kato, H. Sugimoto, *IEEE Photovolt. Special. Conf.* **2016**, 43, 1287.
- [13] C.-Y. Huang, W.-C. Lee, A. Lin, *J. Appl. Phys.* **2016**, 120, 094502.
- [14] S. Kim, J. Nishinaga, Y. Kamikawa, S. Ishizuka, T. Nagai, T. Koida, H. Tampo, H. Shibata, K. Matsubara, S. Niki, *Jpn. J. Appl. Phys.* **2018**, 57, 055701.
- [15] G. Wang, G. Cheng, B. Hu, X. Wang, S. Wan, S. Wu, Z. Du, *J. Mater. Res.* **2010**, 25, 2426.
- [16] B. J. Mueller, M. Mock, V. Haug, F. Hergert, T. Koehler, S. Zweigart, U. Herr, *Thin Solid Films* **2015**, 582, 284.
- [17] J. K. Larsen, J. Keller, O. Lundberg, T. Jarmar, L. Riekehr, J. J. S. Scragg, C. Platzer-Bjorkman, *IEEE J. Photovolt.* **2018**, 8, 604.
- [18] H. Aboulfadl, J. Keller, J. Larsen, M. Thuvander, L. Riekehr, M. Edoff, C. Platzer-Bjorkman, *Microsc. Microanal.* **2019**, 25, 532.
- [19] B. M. Başol, A. Halani, C. Leidholm, G. Norsworthy, V. K. Kapur, A. Swartzlander, R. Matson, *Prog. Photovolt. Res. Appl.* **2000**, 8, 227.
- [20] J. Titus, H.-W. Schock, R. W. Birkmire, W. N. Shafarman, U. P. Singh, *MRS Proc.* **2001**, 668, H1.5.
- [21] J. Keller, O. V. Bilousov, E. Wallin, O. Lundberg, J. Neerken, S. Heise, L. Riekehr, M. Edoff, C. Platzer-Bjorkman, *Phys. Status Solidi A* **2019**, 216, 1900472.
- [22] G. Kresse, J. Furthmüller, *Comput. Mater. Sci.* **1996**, 6, 15.
- [23] G. Kresse, J. Furthmüller, *Phys. Rev. B* **1996**, 54, 11169.
- [24] G. Kresse, J. Hafner, *Phys. Rev. B* **1993**, 47, 558.
- [25] G. Kresse, D. Joubert, *Phys. Rev. B* **1999**, 59, 1758.
- [26] P. E. Blöchl, *Phys. Rev. B* **1994**, 50, 17953.
- [27] J. P. Perdew, K. Burke, M. Ernzerhof, *Phys. Rev. Lett.* **1996**, 77, 3865.
- [28] A. Zunger, S.-H. Wei, L. G. Ferreira, J. E. Bernard, *Phys. Rev. Lett.* **1990**, 65, 353.
- [29] A. van de Walle, P. Tiwary, M. de Jong, D. L. Olmsted, M. Asta, A. Dick, D. Shin, Y. Wang, L.-Q. Chen, Z.-K. Liu, *Calphad.* **2013**, 42, 13.
- [30] N. Saini, J. K. Larsen, K. V. Sopiha, J. Keller, N. Ross, C. Platzer-Bjorkman, *Phys. Status Solidi A* **2019**, 216, 1900492.
- [31] K. V. Sopiha, J. K. Larsen, O. Donzel-Gargand, F. Khavari, J. Keller, M. Edoff, C. Platzer-Bjorkman, C. Persson, J. J. S. Scragg, *J. Mater. Chem. A* **2020**, 8, 8740.
- [32] H. J. Monkhorst, J. D. Pack, *Phys. Rev. B* **1976**, 13, 5188.
- [33] R. Bacewicz, W. Gebicki, J. Filipowicz, *J. Phys.: Condens. Matter.* **1994**, 6, L777.
- [34] D. Papadimitriou, N. Esser, C. Xue, *Phys. Status Solidi B* **2005**, 242, 2633.
- [35] P. D. Paulson, R. W. Birkmire, W. N. Shafarman, *J. Appl. Phys.* **2003**, 94, 879.
- [36] H. Hahn, G. Frank, W. Klingler, A.-D. Meyer, G. Störger, *Z. Anorg. Allg. Chem.* **1995**, 279, 241.
- [37] G. Brandt, A. Räuber, *Solid State Commun.* **1973**, 12, 481.
- [38] T. Wada, N. Kohara, S. Nishiwaki, T. Negami, *Thin Solid Films* **2001**, 387, 118.
- [39] J. Guillemoles, P. Cowache, A. Lusson, K. Fezzaa, F. Boisvion, J. Vedel, D. Lincot, *J. Appl. Phys.* **1996**, 79, 7293.
- [40] C. Stephan, *Dissertation*, Freie Universität Berlin **2011**.
- [41] D. Cahen, R. Noufi, *J. Phys. Chem. Solids* **1991**, 52, 947.
- [42] V. Kumar, B. S. R. Sastry, *J. Phys. Chem. Solids* **2005**, 66, 99.
- [43] A. Jain, S. P. Ong, G. Hautier, W. Chen, W. D. Richards, S. Dacek, S. Cholia, D. Gunter, D. Skinner, G. Ceder, K. A. Persson, *APL Mater.* **2013**, 1, 011002.
- [44] S. Kirklin, J. E. Saal, B. Meredig, A. Thompson, J. W. Doak, M. Aykol, S. Rühl, C. Wolverton, *NPJ Comput. Mater.* **2015**, 1, 15010.
- [45] S. Chen, X. G. Gong, S.-H. Wei, *Phys. Rev. B* **2007**, 75, 205209.
- [46] M. Ishii, K. Shibata, H. Nozaki, *J. Solid State Chem.* **1993**, 105, 504.
- [47] R. Klenk, T. Walter, D. Schmid, H. W. Schock, *Jpn. J. Appl. Phys.* **1993**, 32, 57.
- [48] J. R. Tuttle, D. S. Albin, R. Noufi, *Sol. Cells* **1989**, 27, 231.
- [49] V. Nadenau, D. Hariskos, H.-W. Schock, M. Krcij, F.-J. Haug, A. N. Tiwari, H. Zogg, G. Kostorz, *J. Appl. Phys.* **1999**, 85, 534.
- [50] S. Sanli, *TUprints Technical University of Darmstadt, Darmstadt* **2018**, p. 111.
- [51] A. Virtuani, E. Lotter, M. Powalla, U. Rau, J. H. Werner, M. Acciarri, *J. Appl. Phys.* **2006**, 99, 014906.